Nanoscale

Atomic Thin Telluride Multiheterostructures: Toward Spatial Modulation of Bandgaps

Journal:	*Nanoscale*
Manuscript ID	NR-ART-06-2021-003746.R2
Article Type:	Paper
Date Submitted by the Author:	22-Oct-2021
Complete List of Authors:	Hao, Zheng; University of Illinois at Urbana-Champaign, Electrical and Computer Engineering Xu, Kai; University of Illinois at Urbana-Champaign, Electrical and Computer Engineering Kang, Junzhe; University of Illinois at Urbana-Champaign, Electrical and Computer Engineering Chen, changqiang; University of Illinois at Urbana-Champaign, Frederick-Seitz Materials Research Laboratory Zhu, Wenjuan; University of Illinois at Urbana-Champaign, Electrical and Computer Engineering

Atomic Thin Telluride Multiheterostructures: Toward Spatial Modulation of Bandgaps

Zheng Hao,[1#] Kai Xu,[1#] Junzhe Kang[1#], Changqiang Chen[2], and Wenjuan Zhu[1]*

[1]Electrical and Computer Engineering, University of Illinois at Urbana-Champaign, Urbana, IL 61801
[2]Materials Research Laboratory, University of Illinois at Urbana-Champaign, Urbana, IL 61801

Abstract: Lateral multiheterostructures with spatially modulated bandgaps have great potential for applications in high-performance electronic, optoelectronic and thermoelectric devices. Multiheterostructures based on transition metal tellurides are especially promising due to their wide range of tunable bandgap and rich variety of structure phases. However, the synthesis of telluride-based multiheterostructures remain a challenge due to low activity of tellurium and poor thermal stability of tellurium alloy. In this work, we synthesized monolayer $WSe_{2-2x}Te_{2x}/WSe_{2-2y}Te_{2y}$ $(x > y)$ multiheterostructures in situ using chemical vapor deposition (CVD). Photoluminescence and Raman mapping confirm the spatial modulation of the bandgap in radial direction. Furthermore, field-effect transistors with the channels parallel (type I) and perpendicular (type II) to the multiheterostructure rings were fabricated. Type I transistors exhibit enhanced ambipolar transport, due to the low energy bridges between the source and drain. Remarkably, the photocurrents in type I transistors are two orders of magnitude higher than that in type II transistors, which can be attributed to the fact that the photovoltaic photocurrents generated at the two heterojunctions are summed together in type I transistors, but they cancel each other in type II transistors. These multiheterostructures will provide a new platform for novel electronic/photonic devices with potential applications in broadband light sensing, highly sensitive imaging and ultrafast optoelectronic integrated circuits.

Lateral multiheterostructures with spatially modulated bandgaps have many unique applications, such as color engineered displays, high-performance thermoelectric devices, and tunneling diodes.[1-2] Despite the well-recognized applications, the lack of growth and fabrication technology for such materials has long been the main bottleneck. Lateral epitaxy of III-V materials is restricted by the lattice matching to the substrate. Two-dimensional (2D) materials can address these issues due to their interlayer van der Waals bonding. Various lateral multiheterostructures based on 2D transitional metal dichalcogenides (TMDs) have been synthesized using CVD and metal organic CVD (MOCVD) processes.[3-11] In particular, Zhang et al. shown that TMD multiheterostructures can be formed using a reverse flow during the temperature-swing stage in the sequential vapor deposition growth process.[7] Sahoo et al demonstrated a one-pot synthesis of TMD multiheterostructures by changing the composition of the reactive gas environment in the presence of water vapour.[4] Coherent atomically thin multiheterostructures can also been grown by changing the chalcogen precursors in the MOCVD process.[5] Recently, van der Waals heterostructure arrays between metallic TMDs and semiconducting TMDs were demonstrated using selectively patterning nucleation sites on monolayer or bilayer semiconducting TMDs.[12]

However, most TMD multiheterostructures reported so far were based on binary sulfide and selenide.[13-14] The multiheterostructures based on the ternary tellurides remain unexplored. Due to the low activity of tellurium and poor thermal stability of tellurium alloy, it is very difficult to synthesize tellurium alloy using CVD.[15] Recently, we demonstrated that $WSe_{2-2x}Te_{2x}$ ternary alloy can be synthesized using fast cooling process.[16] Since WTe_2 is a semimetal with zero bandgap, while WSe_2 is a semiconductor with wide bandgap (1.61~1.65 eV for monolayer),[17-18] $WSe_{2-2x}Te_{2x}$ ternary compound has tunable bandgap from ~1.44 eV to ~1.64 eV,[19] covering a broad range of the electromagnetic spectrum.

In this paper, we report the successful growth of monolayer $WSe_{2-2x}Te_{2x}/WSe_{2-2y}Te_{2y}$ multiheterostructures using CVD method. The photoluminescence (PL) line scans manifest periodic modulation of the bandgap as the flake grows laterally from the core to outer rings. Furthermore, transistors were fabricated on monolayer $WSe_{2-2x}Te_{2x}/WSe_{2-2y}Te_{2y}$ multiheterostructures with channel orientation parallel and perpendicular to the telluride rings. We found that the transistor with the channel parallel to the $WSe_{2-2x}Te_{2x}$ ring exhibits stronger ambipolar transport and significantly higher photocurrent as compared to the transistor with the channel perpendicular to the $WSe_{2-2x}Te_{2x}$ ring.

The monolayer $WSe_{2-2x}Te_{2x}/WSe_{2-2y}Te_{2y}$ multiheterostructures were synthesized by precisely controlling the delivery of tellurium precursors and the temperature profile of the furnace. The schematic of the CVD system and the temperature profile of the furnace during the first- and second-round growths of the $WSe_{2-2x}Te_{2x}$ multiheterostructures are in Fig. 1a and 1b. The substrates and WO_3 precursor were placed at the center of the heating zone, while Te and Se precursors were placed near the edge of the heating zone. A movable boat carrying additional Te precursor was placed outside the heating zone of the furnace. In the first-round growth, the temperature was first ramped up from room temperature to 600 ℃ within 20 minutes under 90 sccm Ar flow and low pressure of 25 mTorr. Then the temperature is raised to 760 ℃ within 10 minutes with 9 sccm H_2 flow and was held for 7 minutes for nucleation and diffusion of the

precursors. Next, the furnace was cooled down to 650 ℃, followed by a rapid cooling without flowing H_2. The first-round growth with fast cooling enables the formation of a $WSe_{2-2x}Te_{2x}/WSe_{2-2y}Te_{2y}$ core/shell structure ($x > y$). Subsequently, the second-round growth proceed in situ. The movable crucible with additional Te precursor was pushed into the heating zone using an external magnet. This additional tellurium precursor was used to react with the residual WO_3 and selenium precursors and form the second $WSe_{2-2x}Te_{2x}/WSe_{2-2y}Te_{2y}$ lateral heterostructures. With repeated heating/cooling cycles, $WSe_{2-2x}Te_{2x}/WSe_{2-2y}Te_{2y}$ multiheterostructures were synthesized by sequential edge epitaxy. The optical images of the $WSe_{2-2x}Te_{2x}/WSe_{2-2y}Te_{2y}$ multiheterostructures are shown in Fig. 1c, which reveals the coexistence of alternating $WSe_{2-2x}Te_{2x}$ (dark) and $WSe_{2-2y}Te_{2y}$ (bright) domains. The topography image and the height profile across the flake measured by atomic force microscopy (AFM) are shown in Fig. 1d. The height is uniform across multiple junctions, indicating the formation of seamless lateral multiheterostructures. Note that some pinholes exist on the flakes and substrate. These pinholes may come from the spin-coated perylene-3,4,9,10-tetracarboxylic acid tetrapotassium (PTAS), which was used to aid the nucleation of $WSe_{2-2x}Te_{2x}$ flakes.

Next, the PL and Raman spectra were measured from the center to the edge along the line marked in the optical image shown in Fig. 2a and 2b. Single PL peaks associated with direct excitonic emissions from the flake were observed for $WSe_{2-2x}Te_{2x}/WSe_{2-2y}Te_{2y}$ multiheterostructures (Fig. 2c). The contour plot of the normalized PL intensity as a function of the position from center to edge is shown in Fig 2e. The evolution of the distinct excitonic transitions between each crystal domain can be clearly observed. Across the first junction (from zone 1 to zone 2), the PL peak shifts from 1.44 eV (corresponding to $WSe_{2-2x}Te_{2x}$) to 1.53 eV (corresponding to $WSe_{2-2y}Te_{2y}$). At the second junction (from zone 2 to zone 3), the PL peak jumps back from high energy to low energy. At the interfaces of two zones, the PL spectra are characterized by a co-existence of both peaks, which is due to the laser spot (~1 μm diameter) in the confocal microscope simultaneously probing both sides of the interface. Further, the Raman line scan across the junctions (Fig. 2d) and the contour plot (Fig. 2f) exhibit periodic shift of the Raman peaks. As the laser spot moves from $WSe_{2-2x}Te_{2x}$ (zone 1 and 3) to $WSe_{2-2y}Te_{2y}$ (zone 2 and 4), the E^1_{2g} peak blue-shifts, while the intensity of the A_{1g} peak is enhanced, which are consistent with previous reports.[19] Similar trends were observed in the PL and Raman contour plots taken on other flakes grown in different batches, as shown in Fig. S1. These results indicate that the growth of $WSe_{2-2x}Te_{2x}/WSe_{2-2y}Te_{2y}$ multiheterostructure is repeatable and reproducible. The bandgap modulation of $WSe_{2-2x}Te_{2x}/WSe_{2-2y}Te_{2y}$ multi-heterostructures can be further widened by optimizing the growth parameters. For example, increasing H_2 flow rate during the high-temperature growth period can facilitate the Te atoms to substitute the Se atoms, which will result in higher Te concentration in zone 1 and 3. In addition, decreasing the cooling rate after the high-temperature growth can promote Se substitution of Te atom, which will result in higher Se concentration in zone 2 and 4.

The monolayer $WSe_{2-2x}Te_{2x}/WSe_{2-2y}Te_{2y}$ multiheterostructures enable multichannel devices. As illustrated in Fig. 3a, the transistors with the channels parallel to the $WSe_{2-2x}Te_{2x}$ ring (type I) and perpendicular to the $WSe_{2-2x}Te_{2x}$ ring (type II) were fabricated. These two types of transistors present distinct electrical characteristics as shown in Fig. 3b. The type I transistor exhibits strong

ambipolar transport, while the type II transistor shows p-type transport only. Moreover, the hole current of type I transistor is higher than that of type II transistor. These two types of transistors were fabricated side-by-side on the same flake. The dramatic difference in current transport between these two types of devices can be explained as follows. The tellurium concentration in the $WSe_{2-2x}Te_{2x}$ ring is higher than that in the $WSe_{2-2y}Te_{2y}$ region, which leads to a smaller bandgap in $WSe_{2-2x}Te_{2x}$. In addition, we found in the previous study that the hole Schottky barrier height in $WSe_{2-2x}Te_{2x}$/Pd contact is larger than that in $WSe_{2-2y}Te_{2y}$/Pd contact. Combining this information, we can construct the energy diagrams of the type I and type II transistors, as shown in Fig. 3c. For $WSe_{2-2y}Te_{2y}$/Pd contact, the low Schottky barrier for holes facilitates hole transport, while the large Schottky barrier for electrons limits the electron transport. In contrast, the band alignment between the $WSe_{2-2x}Te_{2x}$ and Pd enables simultaneous transport of both electrons and holes. In type I transistor, the $WSe_{2-2x}Te_{2x}$ and $WSe_{2-2y}Te_{2y}$ sub-channels act as parallel bridges between the source and drain. The carriers can travel via any of these bridges. The Schottky barriers for holes at the $WSe_{2-2x}Te_{2x}$/Pd and $WSe_{2-2y}Te_{2y}$/Pd contacts are both low, so holes can be injected from the drain terminal to all three sub-channels (marked as the red arrows). The Schottky barriers for electrons are low at $WSe_{2-2x}Te_{2x}$/Pd contact, but high at the $WSe_{2-2y}Te_{2y}$/Pd contact, thus the electrons can be injected from source terminal to $WSe_{2-2x}Te_{2x}$ sub-channel (marked as the blue arrow), which lead to strong ambipolar transport. For type II transistor, however, $WSe_{2-2x}Te_{2x}$ and $WSe_{2-2y}Te_{2y}$ zones are in series to each other. The carriers have to be injected through the $WSe_{2-2y}Te_{2y}$/Pd contacts. The large electron barrier at the $WSe_{2-2y}Te_{2y}/P_d$ contact prevents the electron injection and results in p-type transport. In addition, the source and drain terminals are linked via zone 4 outside the channel region can also facilitate the hole transport. Note that hysteresis was observed in double-sweep transfer curves (Fig. S2), which can be attributed to the traps at the dielectric/telluride interfaces.

The photo-response of these two types of transistors were also dramatically different. The time evolution of the drain current were measured under pulses of laser illumination at various gate voltages, shown in Figure. S3. In all cases, the drain current show periodical modulation by the light. The photocurrents were extracted by subtracting the laser-on currents by the laser-off currents and plotted as a function of gate voltage, shown in Fig. 3d. The photocurrent of type I transistor is about two orders of magnitude higher than that of type II transistor. This enhanced photocurrent can be explained by the energy diagrams shown in Fig. 3e-3f. In type II transistors, since the built-in electric fields at the two junctions have opposite directions, the photocurrents due to photovoltaic effect at the two heterojunctions have the same magnitude but opposite polarity. These two current components will cancel each other, as shown in Fig. 3f. The photocurrent due to photoconductive effect at the two heterojunctions are in the same direction. However, the back-to-back heterojunctions acted as series energy barriers and the rectifying effect will degrade the photocurrent. In contrast, for type I transistors, the electrons and holes generated by light at the two heterojunctions will be separated into two sub-channels by the built-in electric field. The electrons will be collected by the $WSe_{2-2x}Te_{2x}$ region and flow along the $WSe_{2-2x}Te_{2x}$ sub-channel to the drain, while holes will flow along the $WSe_{2-2y}Te_{2y}$ sub-channel. Here the electrons generated at the two heterojunctions will flow in the same direction following the lateral electric field between the source and drain. The sum of these two photocurrent components leads to an enhanced overall photocurrent. Furthermore, each heterojunction act as a pseudo-one-dimensional energy

bridge between the source and drain terminals, by which electrons and holes are effectively separated and drifted along the nanowire-like energy bridges. Therefore, the photoresponsivity in type I transistor is significantly improved as compared to type II transistor. The photoresponsivity of the type I transistor can be further enhanced by reducing the density of traps in the dielectrics, minimizing the defects in the alloy, and optimizing the source/drain contacts. These multiheterostructures can also be integrated with ferroelectric materials to construct bipolar transistors and reconfigurable logic transistors.

In summary, lateral monolayer $WSe_{2-2x}Te_{2x}/WSe_{2-2y}Te_{2y}$ multiheterostructures consisting of multiple domains with distinct bandgaps were successfully synthesized using CVD system with magnetic crucibles. The controlled delivery of precursors coupled with temperature modulation enables sequential edge-epitaxy and continuous assembly of planar multi-junctions. The PL spectra manifest periodic modulation of the bandgap in the flake from the center to edge regions. Furthermore, the transistors with the channel parallel to $WSe_{2-2x}Te_{2x}$ rings (type I) exhibit strong ambipolar transport and enhanced photocurrent as compared to the channel perpendicular to the $WSe_{2-2x}Te_{2x}$ ring (type II). Our demonstration of omnidirectional telluride multiheterostructure presents a powerful framework for the epitaxial synthesis of lateral multiheterostructures and the engineering of the local material properties. These multiheterostructures can serve as a unique material platform for novel electronic and optoelectronic devices.

ACKNOWLEDGMENT

The authors would like to acknowledge the support from the Office of Naval Research (ONR) under grant NAVY N00014-17-1-2973 and National Science Foundation (NSF) under grant ECCS 16-53241 CAR.

AUTHOR INFORMATION

[#] Zheng Hao, Kai Xu and Junzhe Kang contributed equally.

* Corresponding Author: Wenjuan Zhu, email: wjzhu@illinois.edu

References:

1. Pan, A. L.; Zhou, W. C.; Leong, E. S. P.; Liu, R. B.; Chin, A. H.; Zou, B. S.; Ning, C. Z., Continuous Alloy-Composition Spatial Grading and Superbroad Wavelength-Tunable Nanowire Lasers on a Single Chip. *Nano Lett* **2009,** *9* (2), 784-788.
2. Ning, C. Z.; Pan, A. L.; Liu, R. B., Spatially Composition-Graded Alloy Semiconductor Nanowires and Wavelength Specific Lateral-Multijunction Full-Spectrum Solar Cells. *Ieee Phot Spec Conf* **2009**, 2289-2292.
3. Li, M. Y.; Shi, Y.; Cheng, C. C.; Lu, L. S.; Lin, Y. C.; Tang, H. L.; Tsai, M. L.; Chu, C. W.; Wei, K. H.; He, J. H.; Chang, W. H.; Suenaga, K.; Li, L. J., NANOELECTRONICS. Epitaxial growth of a monolayer WSe2-MoS2 lateral p-n junction with an atomically sharp interface. *Science* **2015,** *349* (6247), 524-8.
4. Sahoo, P. K.; Memaran, S.; Xin, Y.; Balicas, L.; Gutierrez, H. R., One-pot growth of two-dimensional lateral heterostructures via sequential edge-epitaxy. *Nature* **2018,** *553* (7686), 63-67.
5. Xie, S.; Tu, L.; Han, Y.; Huang, L.; Kang, K.; Lao, K. U.; Poddar, P.; Park, C.; Muller, D. A.; DiStasio, R. A., Jr.; Park, J., Coherent, atomically thin transition-metal dichalcogenide superlattices with engineered strain. *Science* **2018,** *359* (6380), 1131-1136.
6. Zhang, Y.; Yin, L.; Chu, J.; Shifa, T. A.; Xia, J.; Wang, F.; Wen, Y.; Zhan, X.; Wang, Z.; He, J., Edge-Epitaxial Growth of 2D NbS2 -WS2 Lateral Metal-Semiconductor Heterostructures. *Adv Mater* **2018**, e1803665.
7. Zhang, Z.; Chen, P.; Duan, X.; Zang, K.; Luo, J.; Duan, X., Robust epitaxial growth of two-dimensional heterostructures, multiheterostructures, and superlattices. *Science* **2017,** *357* (6353), 788-792.
8. Duan, X.; Wang, C.; Shaw, J. C.; Cheng, R.; Chen, Y.; Li, H.; Wu, X.; Tang, Y.; Zhang, Q.; Pan, A.; Jiang, J.; Yu, R.; Huang, Y.; Duan, X., Lateral epitaxial growth of two-dimensional layered semiconductor heterojunctions. *Nat Nanotechnol* **2014,** *9* (12), 1024-30.
9. Gong, Y.; Lei, S.; Ye, G.; Li, B.; He, Y.; Keyshar, K.; Zhang, X.; Wang, Q.; Lou, J.; Liu, Z.; Vajtai, R.; Zhou, W.; Ajayan, P. M., Two-Step Growth of Two-Dimensional WSe2/MoSe2 Heterostructures. *Nano Lett* **2015,** *15* (9), 6135-41.
10. Gong, Y.; Lin, J.; Wang, X.; Shi, G.; Lei, S.; Lin, Z.; Zou, X.; Ye, G.; Vajtai, R.; Yakobson, B. I.; Terrones, H.; Terrones, M.; Tay, B. K.; Lou, J.; Pantelides, S. T.; Liu, Z.; Zhou, W.; Ajayan, P. M., Vertical and in-plane heterostructures from WS2/MoS2 monolayers. *Nat Mater* **2014,** *13* (12), 1135-42.
11. Zhang, X. Q.; Lin, C. H.; Tseng, Y. W.; Huang, K. H.; Lee, Y. H., Synthesis of lateral heterostructures of semiconducting atomic layers. *Nano Lett* **2015,** *15* (1), 410-5.
12. Li, J.; Yang, X.; Liu, Y.; Huang, B.; Wu, R.; Zhang, Z.; Zhao, B.; Ma, H.; Dang, W.; Wei, Z.; Wang, K.; Lin, Z.; Yan, X.; Sun, M.; Li, B.; Pan, X.; Luo, J.; Zhang, G.; Liu, Y.; Huang, Y.; Duan, X.; Duan, X., General synthesis of two-dimensional van der Waals heterostructure arrays. *Nature* **2020,** *579* (7799), 368-374.
13. Xie, S.; Tu, L.; Han, Y.; Huang, L.; Kang, K.; Lao, K. U.; Poddar, P.; Park, C.; Muller, D. A.; DiStasio, R. A.; Park, J., Coherent, atomically thin transition-metal dichalcogenide superlattices with engineered strain. *Science* **2018,** *359* (6380), 1131.
14. Zhang, Z.; Chen, P.; Duan, X.; Zang, K.; Luo, J.; Duan, X., Robust epitaxial growth of two-dimensional heterostructures, multiheterostructures, and superlattices. *Science* **2017,** *357* (6353), 788.
15. Yun, S. J.; Han, G. H.; Kim, H.; Duong, D. L.; Shin, B. G.; Zhao, J.; Vu, Q. A.; Lee, J.; Lee, S. M.; Lee, Y. H., Telluriding monolayer MoS2 and WS2 via alkali metal scooter. *Nature Communications* **2017,** *8* (1), 2163.
16. Xu, K.; Sharma, A.; Kang, J.; Hu, X.; Hao, Z.; Zhu, W., Heterogeneous Electronic and Photonic Devices Based on Monolayer Ternary Telluride Core/Shell Structures. *Adv Mater* **2020,** *32* (47), 2002548.
17. Yan, T.; Qiao, X.; Liu, X.; Tan, P.; Zhang, X., Photoluminescence properties and exciton dynamics in monolayer WSe2. *Appl Phys Lett* **2014,** *105* (10), 101901.

18. Kumar, A.; Ahluwalia, P. K., Electronic structure of transition metal dichalcogenides monolayers 1H-MX2 (M = Mo, W; X = S, Se, Te) from ab-initio theory: new direct band gap semiconductors. *The European Physical Journal B* **2012,** *85* (6), 186.
19. Yu, P.; Lin, J.; Sun, L.; Le, Q. L.; Yu, X.; Gao, G.; Hsu, C.-H.; Wu, D.; Chang, T.-R.; Zeng, Q.; Liu, F.; Wang, Q. J.; Jeng, H.-T.; Lin, H.; Trampert, A.; Shen, Z.; Suenaga, K.; Liu, Z., Metal–Semiconductor Phase-Transition in WSe2(1-x)Te2x Monolayer. *Adv Mater* **2017,** *29* (4), 1603991.

20. B. Tang, J. Zhou, P. Sun, X. Wang, L. Bai, J. Dan, J. Yang, K. Zhou, X. Zhao, S. J. Pennycook and Z. Liu, Advanced Materials, 2019, 31, 1900862.

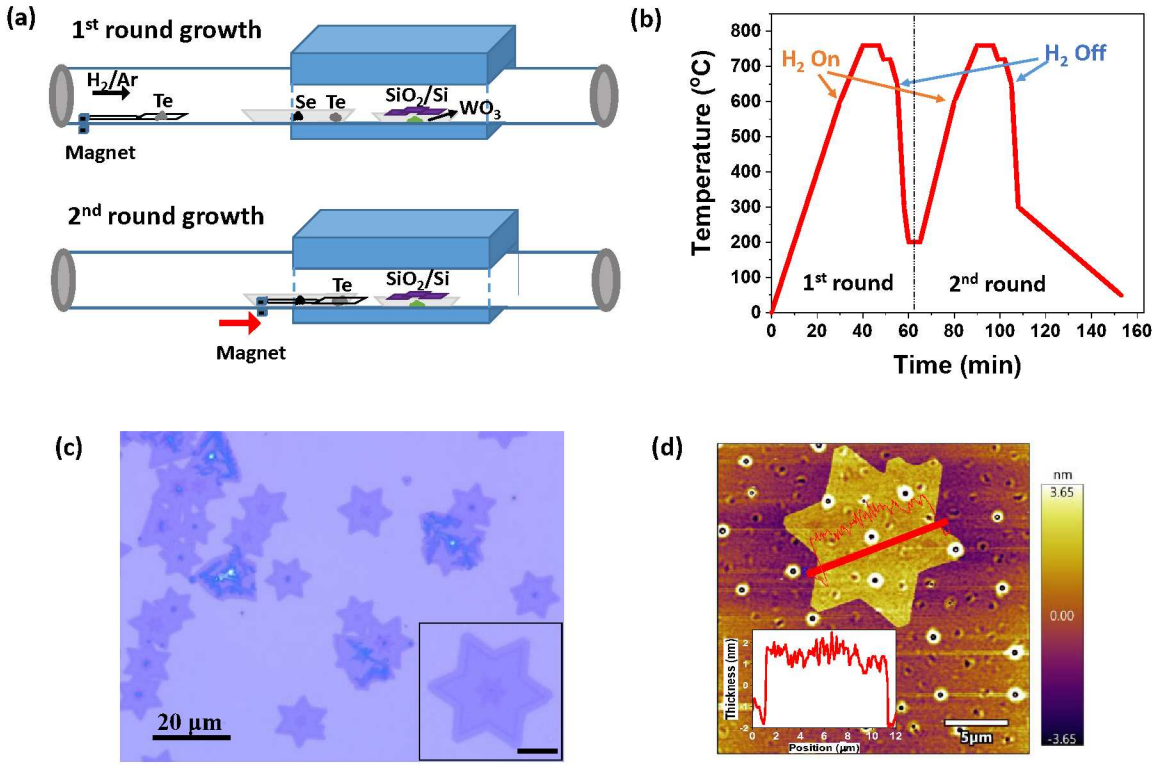

Figure 1. Synthesis of monolayer $WSe_{2-2x}Te_{2x}/WSe_{2-2y}Te_{2y}$ multiheterostructures using CVD system with magnetic controlled crucible. (a) The schematic of the CVD system during the first and second round of growth. (b) The temperature profile of the furnace. (c) The optical image of the multiheterostructures. The inset shows the zoom-in image of a multiheterostructure flake. The scale bar in the inset is 5 μm. (d) AFM topography image of a $WSe_{2-2x}Te_{2x}/WSe_{2-2y}Te_{2y}$ multiheterostructure. The scale bar is 5 μm. The inset shows the height profile across the flake taken along the red line.

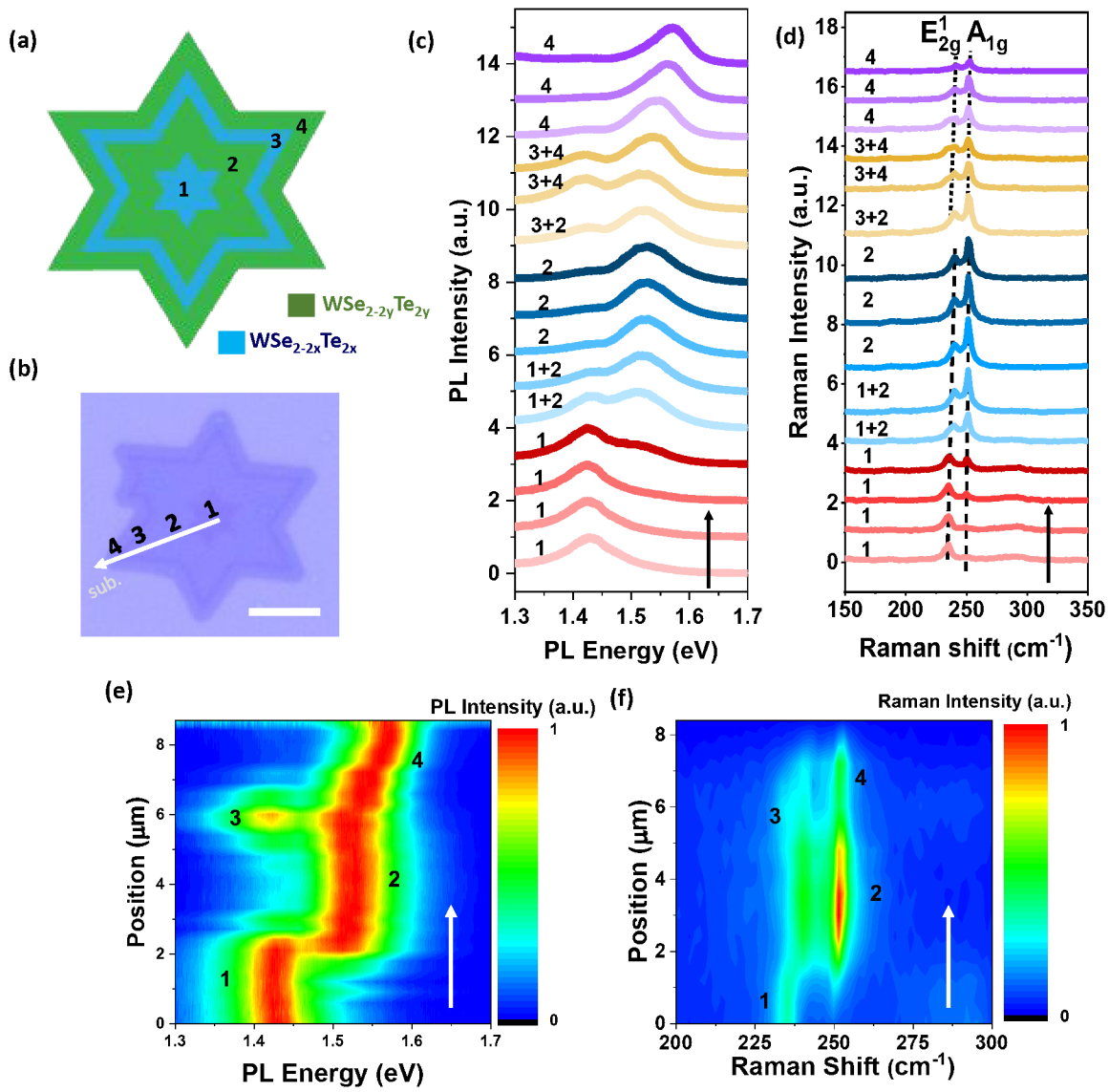

Figure 2. Characterization of monolayer $WSe_{2-2x}Te_{2x}/WSe_{2-2y}Te_{2y}$ multiheterostructures. (a) Illustration and (b) optical image of a $WSe_{2-2x}Te_{2x}/WSe_{2-2y}Te_{2y}$ multiheterostructure structure. The scale bar is 5 μm. (c) PL spectra and (d) Raman spectra taken from the center (zone 1) to edge (zone 4) of the multiheterostructure, as marked in (b). (e) Normalized PL and (f) normalized Raman contour plots along a direction perpendicular to the interfaces, where the arrow indicates the growth direction (from center to edge).

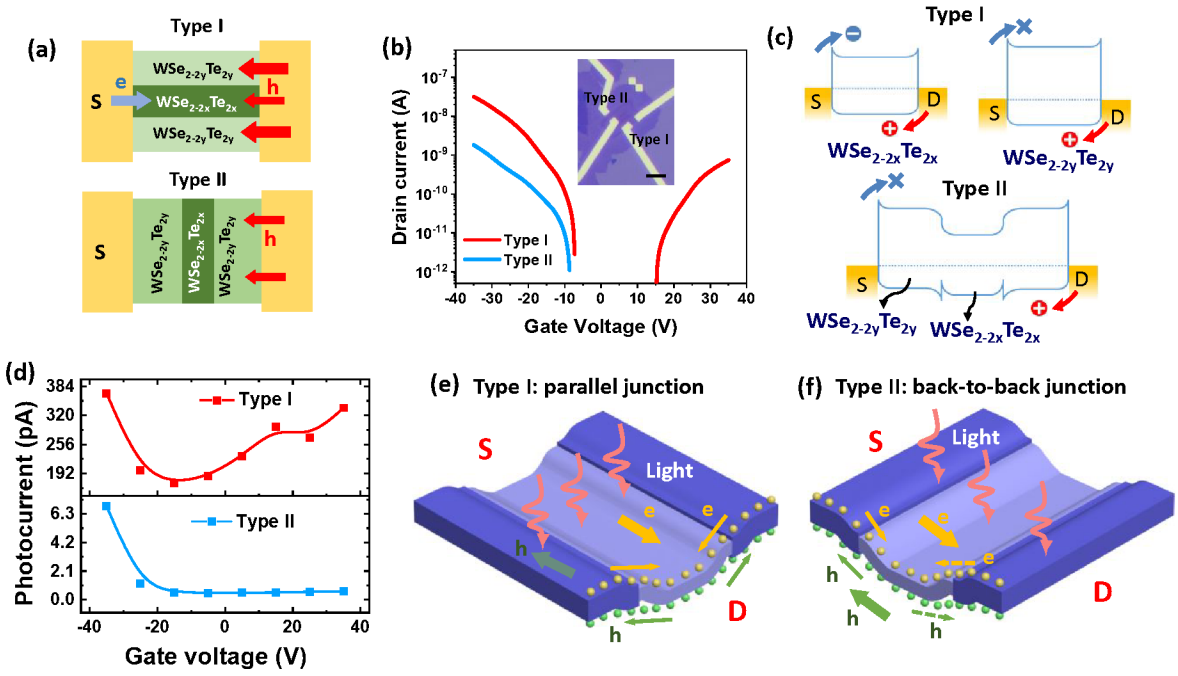

Figure 3. The transistors based on the monolayer $WSe_{2-2x}Te_{2x}/WSe_{2-2y}Te_{2y}$ multiheterostructures. (a) The schematics of two types of transistors: type I transistor has the channel parallel to the $WSe_{2-2x}Te_{2x}$ ring, while type II transistor has the channel perpendicular to the $WSe_{2-2x}Te_{2x}$ ring. The red arrows depict the hole injection, while blue arrow shows the electron injection, when the drain voltage is positive. (b) The transfer curves of the type I and II transistors. Inset: the optical image of the type I and II transistors. The scale bar is 10 μm. (c) Energy diagrams of the type I and II transistors. (d) The photocurrents of the type I and II transistors. The type I transistor exhibits significant higher photocurrent as compared to the type II transistor. The diameter of the laser spot is 10.5 μm. The intensity of the laser is 7.5 W/cm^2. The width and length of the transistor channel are 2 μm. The drain voltage is 1 V. (e) and (f) 3D Energy diagrams for type I and II transistors, respectively. In type I transistor, the photo-generated carriers are separated by the built-in electric field and the carriers are collected along the pseudo-1D channels. In type II transistors, however, the photocurrents due to photovoltaic effect generated at the two heterojunctions cancel each other.